

Titre: High-speed multinozzle additive manufacturing and extrusion
Title: modeling of large-scale microsccaffold networks

Auteurs: Jean-François Chauvette, David Brzeski, lee Lee Hia, Rouhollah D.
Authors: Farahani, Nicola Piccirelli, & Daniel Therriault

Date: 2021

Type: Article de revue / Article


Référence: Chauvette, J.-F., Brzeski, D., Hia, I. L., Farahani, R. D., Piccirelli, N., & Therriault, D.
Citation: (2021). High-speed multinozzle additive manufacturing and extrusion modeling of large-scale microsccaffold networks. Additive Manufacturing, 47, 102294 (11 pages). <https://doi.org/10.1016/j.addma.2021.102294>

 **Document en libre accès dans PolyPublie**
Open Access document in PolyPublie

URL de PolyPublie: <https://publications.polymtl.ca/49781/>
PolyPublie URL:

Version: Version finale avant publication / Accepted version
Révisé par les pairs / Refereed

Conditions d'utilisation: CC BY-NC-ND
Terms of Use:

 **Document publié chez l'éditeur officiel**
Document issued by the official publisher

Titre de la revue: Additive Manufacturing (vol. 47)
Journal Title:

Maison d'édition: Elsevier
Publisher:

URL officiel: <https://doi.org/10.1016/j.addma.2021.102294>
Official URL:

Mention légale:
Legal notice:

High-speed multinozzle additive manufacturing and extrusion modeling of large-scale micro scaffold networks

Jean-François Chauvette¹, David Brzeski¹, Iee Lee Hia¹, Rouhollah D. Farahani¹, Nicola Piccirelli², Daniel Therriault^{1*}

¹Laboratory for Multiscale Mechanics (LM²), Mechanical engineering department, Polytechnique Montréal, Montréal, Québec H3T 1J4, Canada

²Safran Composites, 33 Avenue de la Gare, Itteville, 91760, France

* Corresponding author:

Phone: (514) 340-4711 ext. 4419; Fax: (514) 340-4176

E-mail: daniel.therriault@polymtl.ca

Abstract

In this work, a six-degree-of-freedom (6-DOF) robotic infrastructure is used for the high-speed additive manufacturing (AM) of large-scale networks of high-resolution scaffolds made of microfilaments, referred as micro scaffold networks. The use of a multinozzle printhead, featuring an extrusion nozzle array of 26 cylindrical nozzles of 250 μm inner diameter, enabled the AM of micro scaffolds with very high flow rate (*i.e.*, $> 300 \text{ mm}^3/\text{s}$) and printing speed (*i.e.*, up to 250 mm/s) while preserving fine features. A Multinozzle Extrusion Prediction Model (MEPM), based on capillary rheometry, was developed to predict the extrusion pressure gradient and the overall total volumetric flow rate of the printing process. The MEPM predictions are made as a function of the material used, printing speed and multinozzle printhead configuration (*i.e.*, nozzles inner diameter and number of nozzles). Experimental pressures and flow rates strongly match the MEPM predictions for a printing speed range of 0 to 250 mm/s. The MEPM is also used to explore the design of other multinozzle configurations. The advantages of the high-speed multinozzle AM infrastructure is demonstrated through four case studies. The high-speed printing of micro scaffold network demonstrated a printing speed of up to 250 mm/s, with flow rate of $\sim 319.4 \text{ mm}^3/\text{s}$. The 6-DOF of the robot are used to manufacture a variable pore size micro scaffold network, which shows an achievable inter-filaments spacing of 0 to 750 μm . The printing of a large-scale partitioned micro scaffold network spans over an area of $\sim 9 \times 10^4 \text{ mm}^2$. Finally, a

relatively thick partitioned micro scaffold network is manufactured up to 50 layers (~ 10 mm thick). Findings of this work contribute to the development of multinozzle printheads, high-speed 3D printing and high-resolution micro scaffold manufacturing, which could be targeted for a wide range of applications including sound absorption, smart materials, and tissue engineering.

Keywords

Multinozzle printhead, high-speed 3D printing, large-scale 3D printing, additive manufacturing, extrusion modeling, 6-axis robotic printing.

1. Introduction

Additive Manufacturing (AM), or three-dimensional (3D) printing, is a group of manufacturing methods that allow the realization of complex objects based on the principle of the superposition of layers of material according to the decomposition of a computer-assisted design model [1]. Expanding since the early 1980s [2], AM now offers a broad range of benefits such as low cost, mass optimization, reduction of material losses, a high design freedom and a large diversity of compatible materials [3]. Most common techniques rely on material extrusion (*e.g.*, Fused Filament Fabrication, Direct-Ink-Writing (DIW)). DIW is based on the concept of continuous extrusion of filamentary materials, called ink, through a fine nozzle. Pressure is increased at the inlet of a reservoir by pneumatics, hydraulics, or an endless screw to extrude the material. When using a non-Newtonian shear-thinning ink, the extrusion occurs when the fluid is subjected to a shear stress through the nozzle. The viscosity of a shear-thinning ink decreases with increasing shear rate, generally following a power law, causing the ink to exit the nozzle and solidify on the printing surface to achieve the desired geometry [3–5].

DIW is often used with soft polymers, hydrogels, or other paste-like materials to manufacture compact high resolution scaffolds involving micro-scale features, referred as micro scaffold [6,7], small

complex metallic structures [8] or microfluidic devices [9]. DIW is highly flexible, but is generally limited by a slow to moderate printing speed (~ 1 up to 100 mm/s) which could lead to long printing time, especially for the AM of parts where the printed volume is significantly larger than the nozzle diameter. Bey-Oueslati et al. [10] investigated high-speed DIW using a cylindrical nozzle of 200 μm inner diameter and a low viscosity paste-like organic ink (*i.e.*, mix of wax and petroleum jelly developed in [11]). The authors reported a maximum printing speed of 88 mm/s for the AM of a compact 54-layer microscuffold (~ 19 mm \times 19 mm wide \times ~ 7 mm thick). The printing process required a toolpath approximation using B-splines to reach 88 mm/s, which led to some discrepancies with the expected geometry. Printing speed in DIW is usually constrained by the applied pressure, nozzle tip inner diameter and material used [5,12]. Slightly larger scale DIW was explored by Dubourg-Cassagne [13]. A panel-shaped microscuffold (100 mm \times 40 mm wide \times 12.7 mm thick) was printed using a single nozzle (250 μm inner diameter) with a highly viscous epoxy-based thermosetting polymer. The AM required a period of 10 hours at printing speed of 25 mm/s and refilling the material reservoir (*i.e.*, a 3 cm³ syringe) 12 times.

A multinozzle printhead is a device that allows the simultaneous material extrusion through a series of nozzles arranged in a specific configuration. Multinozzles were used to reduce printing times for structures made of parallel lines [14], print multi-material parts in a single step [15] and print parts at variable resolutions [16]. In general, multinozzle printheads deposit filaments according to the arrangement and orientation of their nozzle array, which limits their use to the production of periodic patterns. Skylar-Scott et al. [15] printed a periodic voxelated prism (~ 40 mm \times 40 mm wide \times 10 mm thick) made of an organic ink (using the same material developed in [11]) of four different colors using a multi-material multinozzle printing head. Their device allowed the AM at a moderate printing speed of 40 mm/s. The multinozzle AM of a large-scale microscuffold (using the same material developed in [11]) was demonstrated by Kranz [17] with a device composed of 64 nozzles of rectangular section of

200 μm \times 200 μm . The printing process produced a 4-layer micro scaffold (616 mm \times 616 mm \times \sim 800 μm thick) at a maximum printing speed of 40 mm/s in 25 minutes using an Aerotech gantry motion system. The use of gantries and 6-axis industrial robots allows the AM of large parts made of concrete [18,19], metals [20–22] and polymers [23–25]. However, as for DIW, the AM of large parts is usually time-consuming, especially to obtain a smooth surface finish [23].

In this work, a custom six-degree-of-freedom (6-DOF) robotic AM infrastructure is combined to a custom-made multinozzle printhead for the high-speed fabrication of relatively large-scale micro scaffold networks. While this paper focuses on the proposed multinozzle AM method, it is planned to exploit the 6-DOF of the robot to print non-planar micro scaffold networks. The main objectives of the current work are: (1) to demonstrate the high-speed multinozzle AM by creating large multifunctional periodic structures and reducing the printing time while maintaining high-resolution features, and (2) to develop a multinozzle extrusion prediction model

2. Experimental methods

2.1. 6-DOF robotic AM infrastructure

A 6-axis industrial robot (Fanuc M-20iB/25, Fanuc Canada Ltd., Canada) equipped with a custom-made multinozzle extrusion printhead (Mékanic – FACMO Chair collaboration, Montreal, Canada) is used for the large-scale AM of micro scaffold networks. Figure 1a presents the 6-DOF robotic AM infrastructure. The 6-axis robot has a maximum reach of 1.8 m and a maximum tool movement speed of 2 m/s, which are exploited for large-scale and high speed AM. The robot can move the printhead mounted on its arm in any required orientation. The robot is a flexible motion system on which various tools up to a maximum weight of 25 kg can be mounted, such as the custom-made multinozzle printhead of 18 kg. The multinozzle printhead is connected to a custom-made hydraulic pressure controller that can produce an extrusion pressure of up to 65 MPa. The printhead is programmed to operate the desired printing speed v . The current printhead is composed of 26 parallel cylindrical nozzles with nominal inner

diameter $D = 250 \mu\text{m}$ and nominal length $L = 6.5 \text{ mm}$, equally distributed side-by-side by a center-to-center spacing $s = 1 \text{ mm}$. The printing speed v is determined by the user input of a desired linear extrusion velocity at the nozzle exit. Pressure is increased in a hydraulic oil, which displaces a piston that pushes the material through the array of nozzles from a 50 cm^3 reservoir, at room temperature. To meet the target printing speed v , the piston's displacement is controlled by a position sensor (Temposonics R-series RH, MTS, NC, USA). Figure 1b shows a close-up view of the multinozzle printhead extrusion. The material is extruded through all 26 nozzles simultaneously, creating a strip of $\sim 25 \text{ mm}$ wide of individual filaments that are deposited on a printing surface in a layer-by-layer fashion. By synchronizing the extrusion printing speed with the movement of the robot tool center point (TCP), located in the center of the nozzle array, the printed filaments diameter d is theoretically equal to D .

At the end of extrusion, a back pressure is applied in order to stop the flow rate, which slightly retracts the piston backward, with the help of a compressed spring installed in an upper part of the piston (not shown in Figure 1). To record the applied pressure gradient required for material extrusion during the print, the back pressure generated by the spring is recorded alone and is then subtracted from the recorded hydraulic pressure data (see additional explanations in Figure S1).

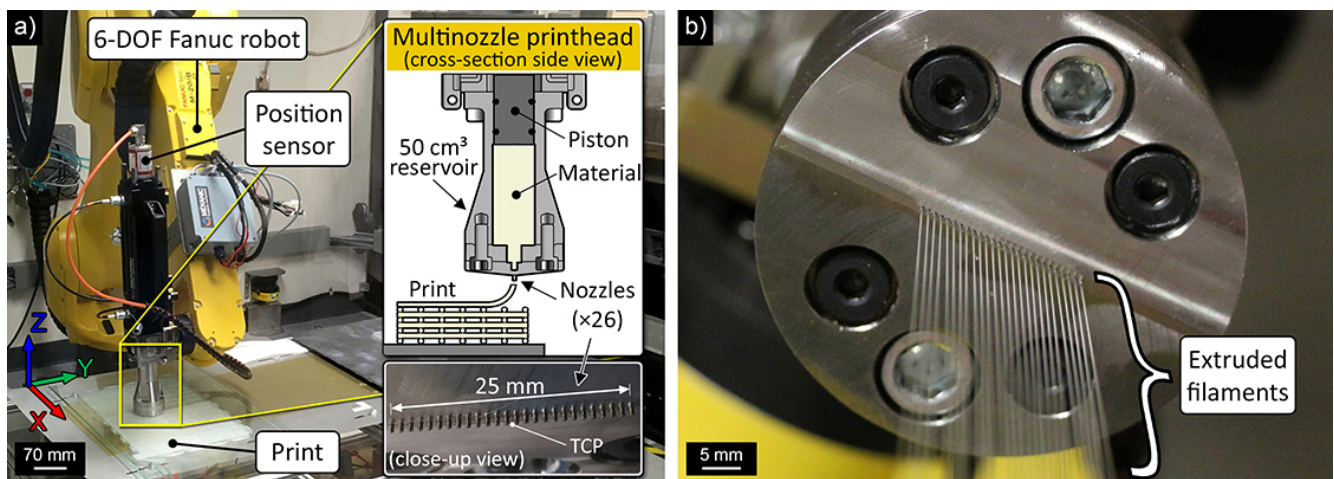


Figure 1. 6-DOF robotic AM infrastructure. a) The material contained in the 50 cm^3 reservoir is pushed by a piston at required pressure through an array of 26 cylindrical nozzles ($D = 250 \mu\text{m}$, $L = 6.5 \text{ mm}$). The piston's course is monitored via a position sensor, which allows accurate pressure setting in order to keep the extrusion flow rate constant. The tool center point (TCP) is located at the center of the nozzle array. b) Close-up view of the multinozzle printhead showing the vertical extrusion of the material through the nozzle array.

2.2. Material preparation

An organic paste-like material (referred as organic ink) developed in [11] was selected because of its low viscosity, shear-thinning behavior, and shape retention at room temperature. The organic ink was prepared according to the method found in [11] using a ratio of 40 wt.% microcrystalline wax (SP-18, Strahl & Pitsch, West Babylon, NY, USA) and 60 wt.% petroleum jelly (Vaseline, Unilever, Canada). The mixture was melted (at ~ 80 °C) and mixed by magnetic stirring for 20 min. The hot ink was then poured directly from a beaker into the 50 cm³ reservoir of the multinozzle printhead and cooled at room temperature after 90 min. The reservoir was closed by inserting the piston in the reservoir chamber inlet using a perforated screw on the piston to let the air escape. The perforated screw was then replaced by an airtight screw to seal the piston-reservoir assembly. Finally, the ink-filled piston-reservoir assembly was mounted on the upper part of the printhead, already fixed on the robot.

2.3. Design and multinozzle AM of microsccaffold networks

The proposed multinozzle AM technique is used for the manufacturing of large networks of interconnected microcaffolds. The method is demonstrated using four different multinozzle AM case studies: High-speed printing of microsccaffold network, variable pore size microsccaffold network, large-scale partitioned microsccaffold network, and thick partitioned microsccaffold network. Figure 2 schematically presents an isometric view of a typical partitioned microsccaffold network of N layers. Microcaffolds (in blue) are as wide as the width of the printhead nozzle array (~ 25 mm) and are printed in an ordered configuration of i rows \times j columns over several layers, in order to generate a periodic structure of interconnected microcaffolds, referred as the network. Detail A shows that each microsccaffold can be partitioned by a separation wall obtained by offsetting the 3D printing toolpath. The separation wall width is expected to be equal to the diameter of a filament d . However, filaments of the wall appear to have an imperfect non-circular shape as presented in the case study (see Section 4.3.3). These walls are intended to separate the volume of air occupied inside each of the microcaffolds, which

could be useful for some applications. In Detail B, the top view of a microsccaffold presents the resulting pore size p (defined as the air gap between filaments from the top view) equal to $750\ \mu\text{m}$ when $d = 250\ \mu\text{m}$ (shown in Detail C). As seen in Detail C, p depends on the center-to-center spacing s (1 mm), between each nozzle, but also the printhead orientation around its axis with respect to the printing direction (see Section 4.3.2). Thus, as shown in Detail D, the toolpath offset must be equal to s to perfectly align the filaments of each microsccaffold and each wall (in red). This pattern leads to each microsccaffold being a square shape of $\sim 26\ \text{mm} \times 26\ \text{mm}$ wide, which corresponds to the total printing width for all 26 filaments ($\sim 25\ \text{mm}$) in addition to a 1 mm offset to generate the partition walls.

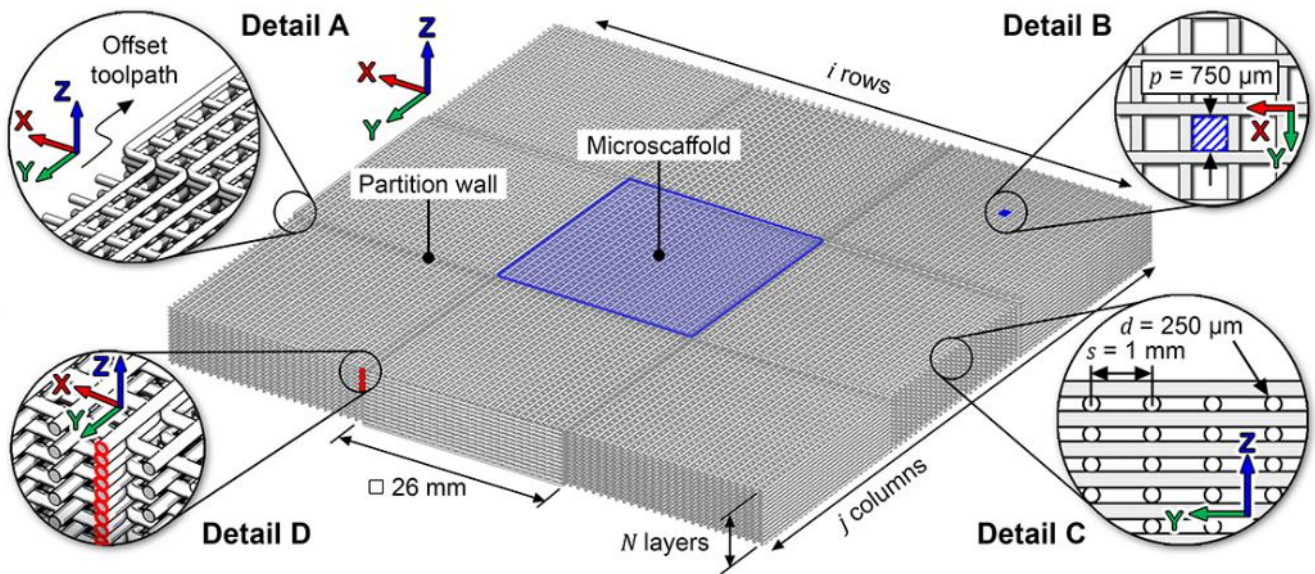


Figure 2. Isometric view of a typical partitioned microsccaffold network ($i \times j$ configuration, N number of layers). Detail A: view of a partition wall made by an offset toolpath. Detail B: top view of the pore size $p = 750\ \mu\text{m}$ (in blue). Detail C: side view of the filaments center-to-center spacing $s = 1\ \text{mm}$ and nominal filament diameter $d = 250\ \mu\text{m}$. Detail D: Cross-sectional view of the filaments stacking in a wall (in red).

The first step in the AM of a typical microsccaffold network consists of generating the toolpath using a custom Python script. The printing speed is programmed from 50 to 250 mm/s and the flow rate is maintained constant via the hydraulic pressure system of the robotic AM infrastructure. The flow rate is continuous from the start up to the end of the deposition. A simple $i \times j$ configuration network of straight parallel filaments is generated following the X axis direction in order to realize the first layer of the

microscaffold network. Then, the printhead rotates at 90° on its Z axis, moves at the beginning of the next layer and is offset in the $+Z$ axis direction of the planar printing surface before printing a second filament network to obtain an $i \times j$ partitioned microscaffold network of 2 layers with perpendicular filaments on top of each other. When changing layers or positioning for the next row or column, the toolpath is slightly cleared of the part to prevent any overlapping of filaments on the manufactured part. The $+Z$ offset is set to 85 % of d , as mentioned in [26], to facilitate the contact between the filaments of the stacked layers. At the end of the second layer, a rotation in the opposite direction to the one of the previous layer is performed on the printhead's Z axis, and the remaining layers are printed in the same fashion as the previous layers. The second step is to convert the toolpath to a proprietary file for Fanuc robots using the software RoboDK's built-in post-processor and then export it into the robot controller. The multinozzle TCP's and the printing surface's reference frame were calibrated using the 3-point method [27]. Finally, the program is launched via the 6-DOF robotic AM infrastructure to allow the fabrication of a microscaffold network.

2.4. Characterization of printed microscaffold networks

The printed microscaffold networks are characterized and analyzed using a stereo microscope (Olympus SZX12, Olympus Corporation, Japan) with software Image Pro Plus (version 7.1) to measure the resulting printed filament diameter and pore size. The robot TCP position, motion speed and printing time are recorded using Labview (2018, National Instrument) with the DigiMetric Robotics Library for Fanuc (DigiMetric GmbH, Germany). Since the organic ink is soft and will not harden, an epoxy encapsulation step is necessary for optical observation of the cross-section and X-ray scan of the network. Using a 10 cm^3 syringe and a $500 \text{ }\mu\text{m}$ inner diameter dispensing nozzle (Nordson EFD, USA), an uncured mix of epoxy resin (Epon 862, Miller-Stephenson, USA) and curing agent (Epikure 3274, Miller-Stephenson, USA) is slowly infiltrated in the network of Case study #4 and cured at room temperature for 48 h in a plastic mold. The encapsulated network is scanned with an X-ray micro

computer tomography scanner (Xradia 520 versa, Zeiss Canada, Canada) at an acceleration voltage of 50 kV (power of 4 W), an objective of 0.4× (field of view of 35 mm) and a voxel size of 34 μm . A total of 4500 projections were recorded at an exposure time of 14 s per scan over a measurement duration of 15h. The 3D scans are analyzed using the software Paraview (version 5.9.0-RC1).

3. Multinozzle Extrusion Prediction Model (MEPM)

3.1. Model development

An analytical Multinozzle Extrusion Prediction Model (MEPM) was developed and programmed using Matlab to predict the required applied pressure gradient for the multinozzle extrusion process and its resulting total flow rate as a function of the printhead's geometry, material used and desired printing speed v . The material is assumed to be incompressible, to be extruded at steady-state and fully developed flow, and the effects of time and temperature on the material's viscosity are not considered. Swelling and nozzle wall slip are also not considered. The nozzles are considered perfectly cylindrical and their length L is considered identical. The pressure gradient is first calculated with an average nozzle diameter to match the programming of the printing-speed-driven pressure controller. Then, using the pressure gradient, volumetric flow rates are recalculated iteratively at each nozzle to reflect geometrical discrepancies between nozzles.

3.1.1. Pressure gradient calculation

The MEPM is based on a similar method proposed by Bruneaux et al. [28] for the applied pressure gradient calculation. The printing speed is considered to be an average velocity at the outlet of all α nozzles, where α is the number of nozzles of the multinozzle printhead. The multinozzle printhead geometry is first defined by measuring the nozzles inner diameter D_i with a stereo microscope (Olympus SZX12, Olympus Corporation, Tokyo, Japan) and software Image Pro Plus (version 7.1). The average nozzle inner diameter D_{avg} is then calculated using D_i . The nozzles geometry is then used with v to estimate the average volumetric flow rate for each nozzle, Q_i , using:

$$Q_i = vA_{\text{avg}} \quad (1)$$

where A_{avg} is the average area of the nozzles calculated with D_{avg} . Using Q_i and D_{avg} , the apparent shear rate inside each nozzle for non-Newtonian fluids, $\dot{\gamma}_i$, is given as:

$$\dot{\gamma}_i = \frac{32Q_i}{\pi D_{\text{avg}}^3} \left(\frac{3 + 1/n}{4} \right) [29] \quad (2)$$

where the term in parenthesis is the Weissenberg–Rabinowitsch correction and n is the material's flow behavior index for a fluid whose viscosity behavior follows a power law model. With $\dot{\gamma}_i$, the non-Newtonian viscosity η_i is calculated for each nozzle using a power law model, given by:

$$\eta_i = K\dot{\gamma}_i^{n-1} [29] \quad (3)$$

where K is the material's flow consistency index. Each parallel nozzle's flow resistance R_i can now be calculated from Hagen-Poiseuille's law for a flow in a pipe and the multinozzle printhead's total equivalent flow resistance R_{eq} is obtained, such as:

$$R_i = \frac{128L\eta_i}{\pi D_{\text{avg}}^4} \left(\frac{3 + 1/n}{4} \right) [29], \quad (4)$$

$$R_{\text{eq}} = \frac{1}{\sum_{i=1}^{\alpha} \frac{1}{R_i}}. \quad (5)$$

Finally, the required applied pressure gradient ΔP is calculated by first summing all Q_i to obtain the total volumetric flow rate Q_{tot} and then multiplying to R_{eq} so that:

$$\Delta P = \sum_{i=1}^{\alpha} Q_i \cdot R_{\text{eq}} = Q_{\text{tot}} R_{\text{eq}} [29]. \quad (6)$$

When all nozzles have the same geometry, the total equivalent flow resistance, given by Equation (5), equals to R_i divided by α , and Q_{tot} , used in Equation (6), is equal to Q_i multiplied by α . Thus, when ΔP is calculated in Equation (6), the terms α cancel each other out (*i.e.*, $\Delta P = Q_i R_i$). Therefore, the calculated pressure for a multinozzle printhead is mathematically the same as for a single nozzle when

all nozzles are in a parallel configuration and feature the same geometry. In reality, diametrical variability inherent to the manufacturing of a multinozzle printhead will result in a unique resistance R_i and a different flow rate Q_i for each nozzle in Equation (4). Hence, the flow rates Q_i must be recalculated for each nozzle according to the applied pressure calculated in Equation (6) and then summed together to obtain the actual Q_{tot} .

3.1.2. Total volumetric flow rate calculation

For the total flow rate calculation, the MEPM uses a similar method proposed by Kranz [17]. Since ΔP is uniform at the inlet of each nozzle but the nozzles real inner diameter D_i vary from its theoretical value, v cannot be assumed to be the same at the outlet of each nozzle. Every nozzle's volumetric flow rate Q_i is no longer an average and is recalculated. Q_i depends on ΔP and ΔP depends on η_i . Every Q_i has to be recalculated iteratively, because η_i depends on $\dot{\gamma}_i$ (and therefore Q_i). For each nozzle, Q_i is used as a first guess $Q_{i,\text{guess}}$. Then, using $Q_{i,\text{guess}}$ and the experimentally measured D_i in Equation (2), a new $\dot{\gamma}_i$ is calculated and reinserted into Equation (3) to obtain η_i . Each nozzle's flow resistance R_i is recalculated using D_i in Equation (4). R_i is used directly with the previously calculated ΔP to obtain a new flow rate for each nozzle, given by:

$$Q_{i,\text{new}} = \Delta P / R_i . \quad (7)$$

Convergence is verified between the new flow rate $Q_{i,\text{new}}$ and the first $Q_{i,\text{guess}}$, using:

$$\Delta Q_i = \frac{|Q_{i,\text{new}} - Q_{i,\text{guess}}|}{Q_{i,\text{guess}}} < 10^{-4} . \quad (8)$$

If the variation ΔQ_i does not meet the convergence condition (reported in [17]), the new flow rate $Q_{i,\text{new}}$ becomes the new $Q_{i,\text{guess}}$ and is reinserted into Equation (2) for another cycle until ΔQ_i becomes smaller than the convergence condition. Once the iterative process converges for all nozzles, each $Q_{i,\text{new}}$ is

summed to obtain the new total volumetric flow rate Q_{tot} (see individual flow rates comparison in Figure S2).

3.2. Model comparison with results from the literature

Extrusion pressures as a function of the printing speed are extracted for two materials taken from the literature to compare with the MEPM predictions. Using the extracted viscosity data (n and K parameters) from [28], the MEPM is used with the reported single nozzle geometry ($\alpha = 1$, $D = 510 \mu\text{m}$, $L = 18.87 \text{ mm}$) for the organic ink developed in [11] using the reported printing speed range of 0 to $\sim 45 \text{ mm/s}$. Using the viscosity data (n and K parameters) from [30], the MEPM is used with the reported single nozzle geometry ($\alpha = 1$, $D = 200 \mu\text{m}$, $L = 12.24 \text{ mm}$) for dissolved polylactide acid (PLA) ink used in Solvent-Cast 3D printing using the reported printing speed range of 0 to $\sim 26 \text{ mm/s}$.

3.3. Multinozzle data acquisition and extrusion prediction

Using a custom data-acquisition interface programmed in Labview (2018, National Instrument), the multinozzle printhead applied pressure gradient is recorded for printing speed setpoints of $v = 50, 100, 150, 200$ and 250 mm/s using the organic ink. The maximum reachable printing speed is 250 mm/s due to the maximum displacement speed of the piston pushing the ink. The recorded pressure gradients are compared to the pressure predicted by the MEPM using a power law viscosity model with $n = 0.468$ and $K = 604 \text{ Pa}\cdot\text{s}^n$ (see viscosity profile in Figure S3), a multinozzle configuration of $\alpha = 26$, $L = 6.5 \text{ mm}$, and the measured nozzles inner diameter D_i . For experiments at printing speed of 50 and 250 mm/s , the total mass of the micro scaffold networks is weighed using a precision scale (EP6501 Explorer Pro, Ohaus Corporation, USA). For experiments at printing speed of $100, 150$ and 200 mm/s , the organic ink is extruded in a beaker. No specific geometries were printed, and the extruded ink collected in the beaker was weighed using the same precision scale. The overall mass flow rate is calculated by dividing the total mass of extruded material over the printing time and then converted to the overall volumetric flow rate Q_{exp} by dividing the estimated organic ink density (estimated using the material components

datasheet and ink composition, see Q_{exp} calculation steps in Table S1). The overall volumetric flow rate Q_{exp} is then compared to Q_{tot} , predicted by the MEPM using the organic ink's rheological properties and the nozzles geometry.

4. Results and discussion

4.1. Design exploration of multinozzle configurations

The MEPM could be used to explore different multinozzle configurations. Figure 3a shows a log-log chart of the applied pressure prediction as a function of the printing speed for four multinozzle configurations of $\alpha = 26$ nozzles with different inner diameter ($D = [100, 250, 500, 750] \mu\text{m}$ and $L = 6.5$ mm). Figure 3b shows a log-log chart of the total volumetric flow rate prediction for the same four multinozzle configurations as in Figure 3a as a function of the printing speed. Figure 3c shows a log-log chart of the total volumetric flow rate prediction as a function of the printing speed for five multinozzle configurations with different number of nozzles ($\alpha = [1, 4, 10, 26, 50]$, $D = 250 \mu\text{m}$, $L = 6.5$ mm). With the established maximum displacement speed of the piston, the maximum printing speed v_{max} is calculated for each configuration by assuming mass conservation through all nozzles and the MEPM is used to compute the applied pressure gradient ΔP and total volumetric flow rate Q_{tot} for $v = 0$ mm/s to v_{max} for each configuration.

4.1.1. Effect of nozzles inner diameter

Reducing the nozzles inner diameter increases the required applied pressure, which also increases the reachable v_{max} . Using the current hydraulic pressure controller with 26 nozzles of $D = 100 \mu\text{m}$, v_{max} would be reached at 1562 mm/s at a pressure of 42.9 MPa for the organic ink, which is under the maximum allowable pressure $P_{\text{max}} = 65$ MPa. Larger nozzles diameter, such as $D = 500 \mu\text{m}$ and $D = 750 \mu\text{m}$, require a lower ΔP but at the cost of smaller v_{max} (*i.e.*, < 100 mm/s) and printing precision. For every nozzle diameter scenario, a maximum Q_{tot} of 319 mm³/s can be achieved at different values of

v_{\max} with the current pressure controller. For a fixed Q_{tot} , reducing D increases v_{\max} . For a fixed printing speed, the use of larger nozzles increases the flow rate while smaller nozzles reduce it.

4.1.2. Effect of the number of nozzles in parallel

For any given printing speed, the flow rate is directly proportional to α , and the applied pressure is the same regardless of the number of nozzles (see Section 3.1.1). The flow rate is linearly dependant on the printing speed. Using a single nozzle ($\alpha = 1$), the theoretical maximum printing speed is equal to 6500 mm/s for the maximum reachable $Q_{\text{tot}} = 319 \text{ mm}^3/\text{s}$ (with $\Delta P = 21.8 \text{ MPa}$). The necessity to match the 6-axis robot tool movement speed in this work limits v_{\max} to $v_{\max, \text{robot}} = 2000 \text{ mm/s}$. The number of nozzles with $D = 250 \text{ }\mu\text{m}$ that a multinozzle printhead must contain to tend toward this printing speed limit while reaching the maximum $Q_{\text{tot}} = 319 \text{ mm}^3/\text{s}$ is $\alpha = 4$ ($v_{\max} = 1625 \text{ mm/s}$, $\Delta P = 11.5 \text{ MPa}$). Such a high speed might be unattainable for short distance printing, as the 6-axis robot has to consider the weight of the multinozzle printhead during acceleration and deceleration [24]. On the opposite side of the chart, the use of 50 nozzles would reduce v_{\max} down to 130 mm/s and ΔP to 3.6 MPa. The manufacturing of a multinozzle printhead containing a high number of nozzles is more likely to cause more geometrical disparities between them.

4.1.3. Current multinozzle configuration

The current multinozzle configuration is shown in red on Figure 3. A compromise of $\alpha = 26$ nozzles at $D = 250 \text{ }\mu\text{m}$ was deemed appropriate for the AM of microsc scaffold networks presented in this work, allowing a Q_{tot} of $319 \text{ mm}^3/\text{s}$ at $v_{\max} = 250 \text{ mm/s}$, requiring a maximum $\Delta P = 4.8 \text{ MPa}$ using organic ink. The current multinozzle configuration is suitable for manufacturing the small features (*i.e.*, filaments, pore size and wall) of the microsc scaffold structures in this work.

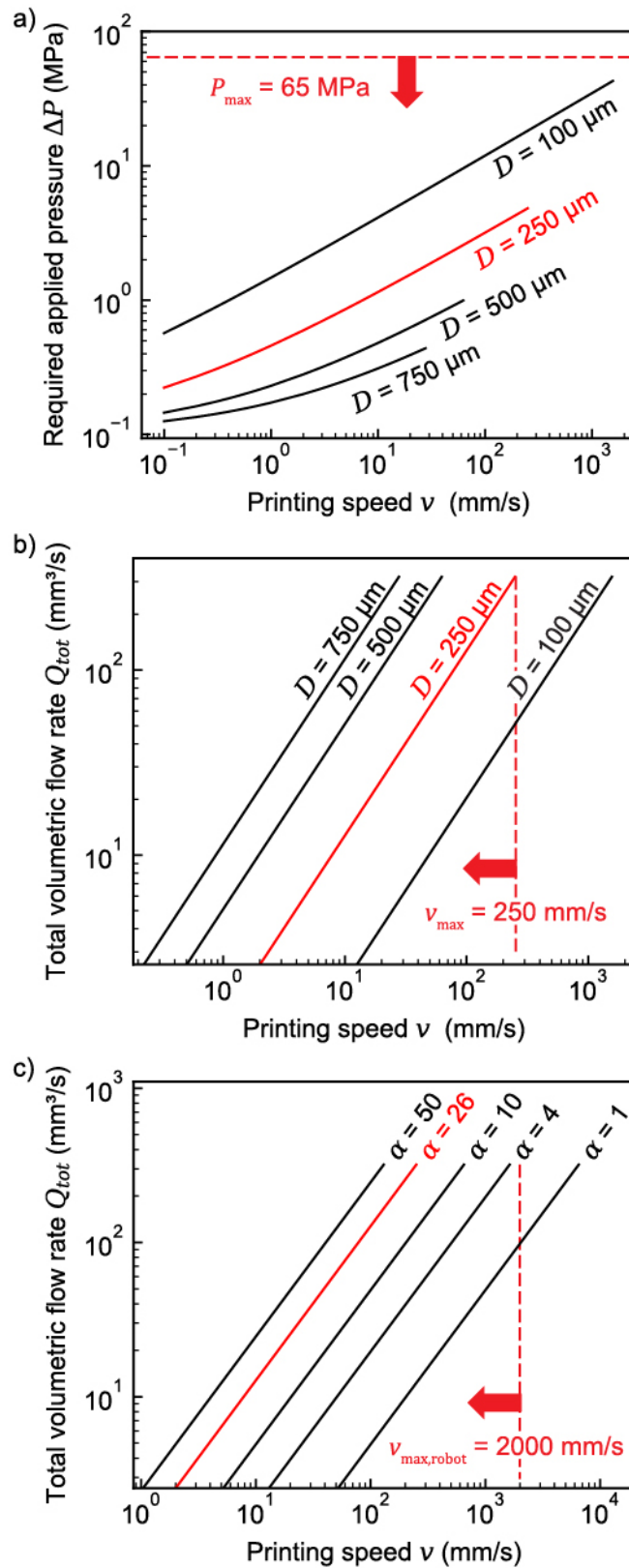


Figure 3. Multinozzle extrusion prediction modeling charts for organic ink. The current infrastructure parameters are shown in red. a) Applied pressure prediction for four multinozzle configurations with different nozzles inner diameter ($\alpha = 26$, $D = [100, 250, 500, 750] \mu\text{m}$, $L = 6.5 \text{ mm}$). The maximum extrusion pressure (65 MPa) is not reached with the use of organic ink

(red dotted line). b) Total volumetric flow rate prediction for four multinozzle configurations with different nozzles inner diameter ($\alpha = 26$, $D = [100, 250, 500, 750] \mu\text{m}$, $L = 6.5 \text{ mm}$). The maximum reachable printing speed for the configuration used in this work ($D = 250 \mu\text{m}$) is 250 mm/s due to the printhead maximum piston displacement speed. c) Total volumetric flow rate prediction for five multinozzle configurations with different number of nozzles ($\alpha = [1, 4, 10, 26, 50]$, $D = 250 \mu\text{m}$, $L = 6.5 \text{ mm}$). The 6-axis robot maximum tool movement speed limits the printing speed at 2000 mm/s.

4.2. Prediction of single and multinozzle extrusions

4.2.1. Model comparison using single nozzle configuration

Figure 4a presents the applied pressure gradient calculated using the MEPM as a function of the printing speeds, single nozzle geometries and rheological data reported in [28,30]. Experimental values from [28,30] were plotted on the same graph and compared with the predictions from the MEPM. Predictions for the organic ink used in [28] show a mean absolute error (MAE) of $\sim 0.045 \text{ MPa}$ (mean relative error (MRE) of 3.5 %) with the authors' results for all printing speeds. Similarly, the predictions for dissolved PLA ink [30] exhibit a slightly higher ΔP to allow extrusion at the given printing speeds, with a MAE $\sim 0.075 \text{ MPa}$ and MRE of 10.8 %. The printing speeds reported by the authors are estimated by measuring the extruded filaments diameter following the application of a known pressure gradient (following the method explained in [28]). Inversely, the printing speeds used in the MEPM are known, and the pressures are measured. Both calculation methods introduce different effect from the experimental errors, which could explain the errors between the predictions and the authors results. The MEPM works as intended for single nozzle geometries and is suitable to predict the applied pressure, at any printing speed, of a wide range of non-Newtonian fluids.

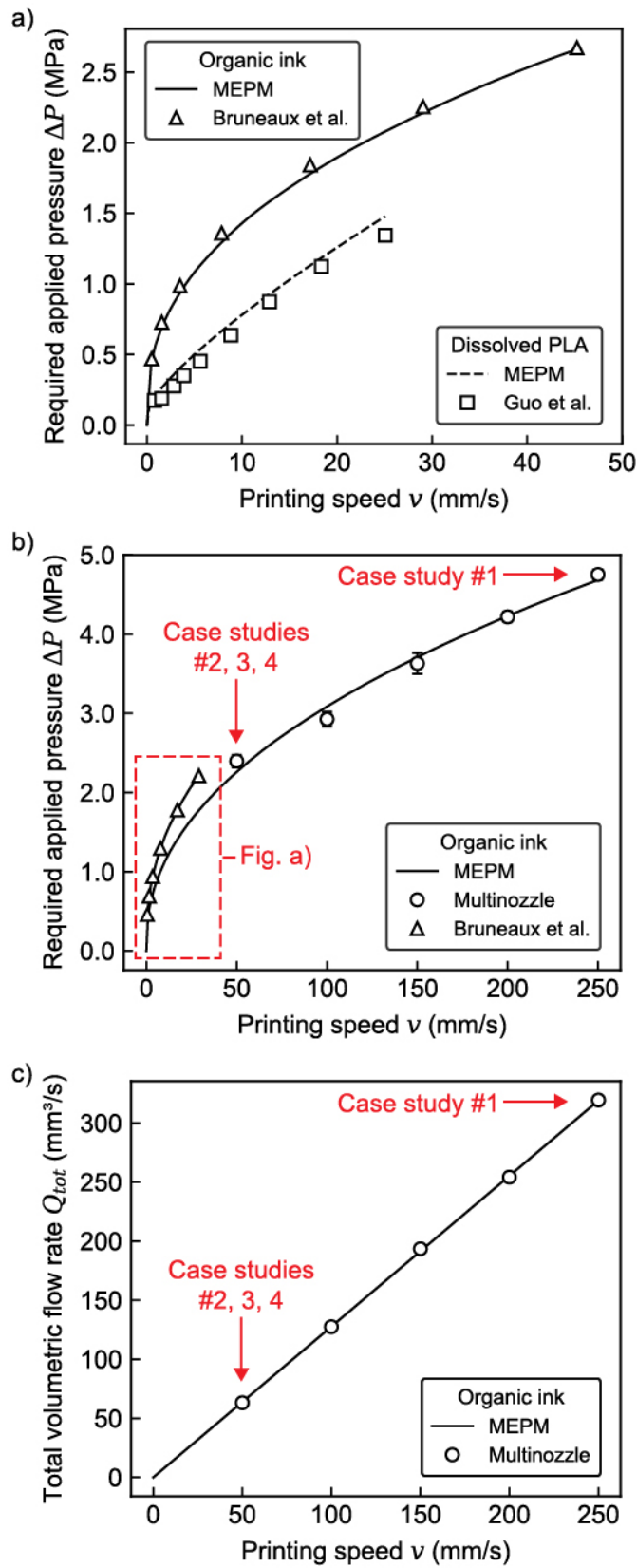


Figure 4. a) Comparison of the MEPM and experimental values from the literature for single cylindrical nozzle extrusion ($\alpha = 1$, $D = 510 \mu\text{m}$, $L = 18.87 \text{ mm}$) of organic ink (60/40 wt.%) [28] and single cylindrical nozzle extrusion ($\alpha = 1$, $D = 200 \mu\text{m}$, $L = 12.24 \text{ mm}$) of dissolved Poly(lactic acid) (PLA, 20 wt.%) for solvent-cast 3D printing [30]. b) Applied pressure

prediction and experimental results for multinozzle (cylindrical, $\alpha = 26$, $D = 250 \mu\text{m}$, $L = 6.5 \text{ mm}$) extrusion of organic ink at $v = 50, 100, 150, 200$ and 250 mm/s . Error bars represent the 95 % confidence interval. c) Total volumetric flow rate prediction and experimental results from the experiments in b).

4.2.2. Applied pressure prediction using multinozzle configuration

Figure 4b shows the MEPM predictions and experimental measurements of the applied pressure gradient as a function of the printing speed and multinozzle geometry ($D_{\text{avg}} = 255 \mu\text{m}$) for the extrusion of the organic ink. The maximum printing speed of 250 mm/s requires a constant applied pressure of 4.75 MPa (standard deviation $\sigma = 0.05 \text{ MPa}$), at which Case study #1 was manufactured (see Section 4.3). The printing speed was reduced to 50 mm/s and Case study #2, #3 and #4 were manufactured with a constant applied pressure of 2.40 MPa ($\sigma = 0.07 \text{ MPa}$). Printing speeds of 100 mm/s (2.93 MPa , $\sigma = 0.08 \text{ MPa}$), 150 mm/s (3.63 MPa , $\sigma = 0.12 \text{ MPa}$) and 200 mm/s (4.22 MPa , $\sigma = 0.06 \text{ MPa}$) were also investigated. The reported values represent the average pressure recorded over several experiments and the error bars represent the 95 % confidence interval of each printing speed. Values of Figure 4a are superimposed on top of the plot for comparison between single nozzle and multinozzle. Pressures reported by Bruneaux et al. [28] and calculated using the MEPM are coherent with measured and predicted pressures of the multinozzle printhead. Pressures in the domain of Figure 4a (*i.e.*, 0 to $\sim 50 \text{ mm/s}$) are slightly higher than the predicted pressures in the same domain of Figure 4b. The applied pressure for a single nozzle should mathematically be the same as the applied pressure for a multinozzle if all nozzles share the same inner diameter and length as the single nozzle. For the same material, the power law viscosity parameters n and K must be identical. Thus, the shift between the two organic ink curves could be explained by geometrical differences between the single nozzle and multinozzle, but mostly by the approximation of the authors' actual material viscosity estimated by n and K . These parameters are directly proportional to the pressure calculation and are different in both cases. The MEPM is therefore able to predict the required pressure to allow extrusion of organic ink for any given printing speed.

4.2.3. Total volumetric flow rate prediction using multinozzle configuration

Figure 4c shows the predictions and the experimental measurements of the total volumetric flow rate for the experiments presented in Figure 4b. At a printing speed of 250 mm/s, an overall total volumetric flow rate $Q_{\text{tot}} \sim 319.4 \text{ mm}^3/\text{s}$ ($\sigma = 2.3 \text{ mm}^3/\text{s}$) is required to manufacture Case study #1. At a printing speed of 50 mm/s, $Q_{\text{tot}} \sim 63.2 \text{ mm}^3/\text{s}$ ($\sigma = 1.9 \text{ mm}^3/\text{s}$) is required to manufacture Case study #2, #3 and #4. The experimental results are strongly aligned with the MEPM predictions for $v = 0$ to 250 mm/s. The MEPM is therefore able to accurately predict the total volumetric flow rate generated by the extrusion process of the multinozzle printhead.

4.3. Case studies: Multinozzle AM of periodic microsccaffold networks

4.3.1. Case study #1: High-speed printing of microsccaffold network

Figure 5 shows a 5-layer microsccaffold network (9×15 configuration, without partition walls) made of the organic ink. The target printing speed $v = 250 \text{ mm/s}$ is set in order to print at maximum flow rate $Q_{\text{tot}} \sim 319.4 \text{ mm}^3/\text{s}$ at an applied pressure of 4.75 MPa (see Sections 4.2.2 and 4.2.3). Figure 5a shows a top view of the entire printed microsccaffold network. The scalebar represents the total printing width of a typical microsccaffold (*i.e.*, 26 mm). The result is one large $225 \text{ mm} \times 375 \text{ mm} \times 1 \text{ mm}$ microsccaffold network composed of 234×390 filaments wide, that weighs approximately 27.7 g in total, and requires approximately 1 minute 36 seconds to manufacture (see supplementary Video S1). Assuming the same geometrical specifications, dimensions, and extruded mass, printing this microsccaffold network using a single nozzle (with $D = 250 \text{ }\mu\text{m}$ and $L = 6.5 \text{ mm}$) would take ~ 41 minutes (for $\alpha = 1$, $v_{\text{max}} = 250 \text{ mm/s}$ and $Q_{\text{tot}} \sim 12.3 \text{ mm}^3/\text{s}$, see Figure 3c). Figure 5b presents a close-up top view of the overall network. The structure is composed of smooth parallel lines, which are perpendicularly overlapped and connected between layers. Figure 5c presents a $\times 25$ magnification image, where the average measured filaments diameter \bar{d} is $255 \text{ }\mu\text{m}$ ($\sigma = 15 \text{ }\mu\text{m}$, $d_{\text{theo}} = 250 \text{ }\mu\text{m}$) and the average pore size \bar{p} is $736 \text{ }\mu\text{m}$ ($\sigma = 21 \text{ }\mu\text{m}$, $p_{\text{theo}} = 750 \text{ }\mu\text{m}$).

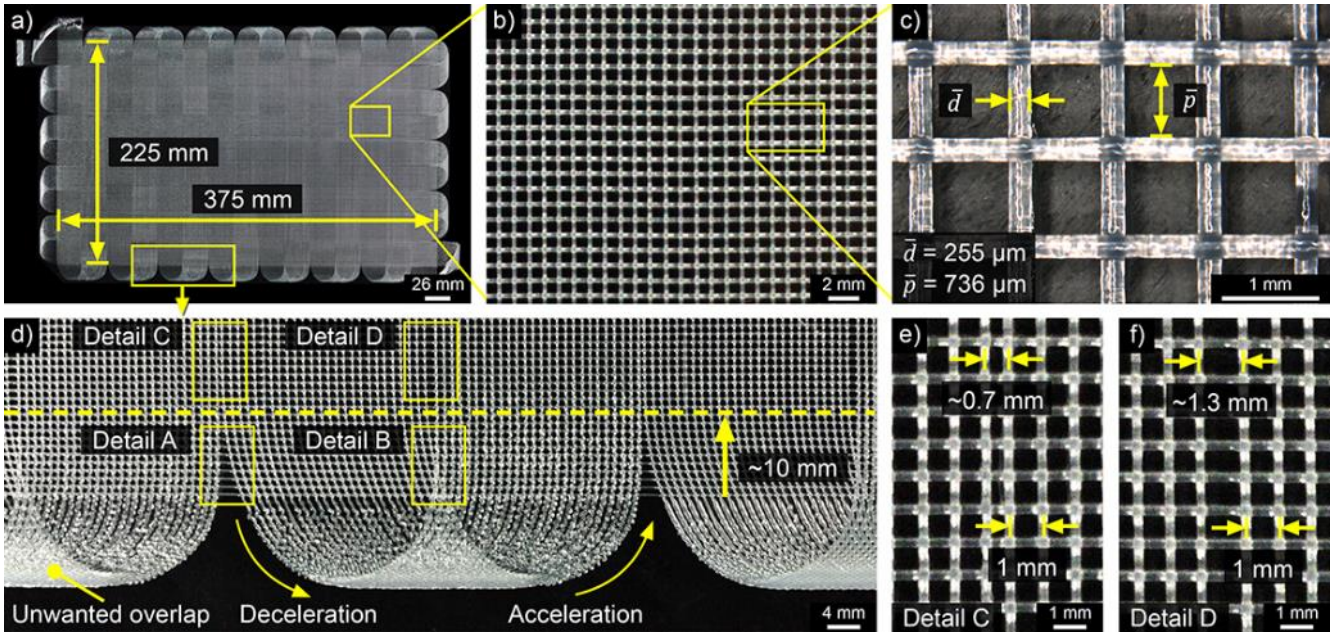


Figure 5. 5-layer microsccaffold network (9×15 configuration) printed at 250 mm/s (~ 1 min 36 s) for a total of 234×390 filaments wide. a) Top view of the entire print. b) Close-up top view of the microsccaffold network. c) $\times 25$ magnification image of the microsccaffold filament stacking showing the average filaments diameter $\bar{d} = 255 \mu\text{m}$ and average pore size $\bar{p} = 736 \mu\text{m}$. d) Close-up view of the transition between two columns displaying a toolpath rounding, which reduces the microsccaffold network size by 10 mm. Focus on details of print defects A, B, C and D. e-f) Close-up views of the spacing between printed columns (Details C, D).

Figure 5d shows a close-up view of a transition between columns, where the printhead's position must be laterally shifted for the next column deposition. Due to the incapacity of the printhead to momentarily stop the extrusion before printing the next row or column, a toolpath clearance is required to avoid overlapping filaments on the network. To perform the toolpath clearance, the robot must reach a point coordinate outside of the network. Then, to print the next row or column, the robot has to shift its position and go the opposite direction with respect to the last printed direction. Although the robot is programmed to reach the target motion speed of 250 mm/s, maintaining this speed is difficult when the printhead changes direction. For a sharp turn ($\leq 90^\circ$), the kinematic model of the robot forces the printhead TCP to slow down and round the toolpath before accelerating again [31]. In the process, the printhead rotation does not change and some filaments overlap each others, creating unwanted overlap features around the network. Moreover, by rounding the toolpath when slowing down from $v = 250$ mm/s, the robot engages the curve too early which jeopardizes the filament stacking of the

microscaffold network (Details A and B). Ruining the perpendicularity of the filaments stacking reduces the overall network dimensions by approximately 10 mm on each side (see the dotted line). The pores size in Details A and B are also affected because of the changing angle between the multinozzle orientation with respect to its printing direction. Shifting the robot's position also causes a positioning error from one column to another (Detail C and D). Figure 5e shows a close-up on Detail C, where the spacing between two printed columns is ~ 0.7 mm and Figure 5f shows a close-up on Detail D, where the spacing is now ~ 1.3 mm. It appears that the position of the TCP is shifted by 0.3 mm between rows and columns. The shift of the TCP position seems to be repeated throughout the microscaffold network and is possibly due to the weight of the multinozzle (18 kg), which is closed to the maximum payload capacity (25 kg). A toolpath compensation could be programmed to adjust the TCP position.

Case study #1 demonstrates the possibility of high-speed AM ($v_{\max} = 250$ mm/s) of a large, structured microscaffold network ($225 \text{ mm} \times 375 \text{ mm} \approx 8.4 \times 10^4 \text{ mm}^2$) at a flow rate of $Q_{\text{tot}} \sim 319.4 \text{ mm}^3/\text{s}$, with an applied pressure of 4.75 MPa. In [17], a multinozzle with 64 smaller rectangular nozzles of $200 \mu\text{m} \times 200 \mu\text{m}$ was used to manufacture a very similar, but larger 4-layer microscaffold ($3.8 \times 10^5 \text{ mm}^2$) made of the same organic ink at a slower printing speed $v_{\max} = 40$ mm/s and a lower flow rate $Q_{\text{tot}} \sim 102 \text{ mm}^3/\text{s}$ (with a higher pressure of 5.17 MPa). The printed area is ~ 4.5 times larger, one layer less, required 25 minutes to print and was printed with smaller nozzles. By comparing with the maximum flow rate of the current multinozzle, a similar microscaffold could theoretically be printed in 8 minutes (~ 3 times faster) with the proposed method and custom infrastructure.

4.3.2. Case study #2: Variable pore size microscaffold network

Figure 6 shows a 2-layer microscaffold network (3×5 configuration) made of the organic ink with variable pore size on its second layer. The target printing speed is set to $v = 50$ mm/s ($Q_{\text{tot}} \sim 63.2 \text{ mm}^3/\text{s}$) at an applied pressure of 2.4 MPa. Figure 6a shows the printing of the entire microscaffold network (see supplementary Video S2). The pore size on the second layer is controlled by rotating the multinozzle

printhead around its Z axis. The angle θ at which the printhead is rotated is the angle between the multinozzle array orientation and the X axis, perpendicular to the printing direction (Y axis). The angle θ is gradually increased for each column of the second layer from 0° to 30° , 45° , 60° and 75.5° , respectively. Figure 6b shows four $\times 25$ magnification images of the micro scaffold at $\theta = 30^\circ$, 45° , 60° and 75.5° . The average experimental pore size \bar{p} decreases while θ increases, until θ reaches 75.5° , at which point the filaments appear to be printed side by side with no spacing between them. The theoretical pore size p_{theo} can be calculated by:

$$p_{\text{theo}} = s \cdot \cos\theta - d. \quad (9)$$

With the current multinozzle configuration, angle $\theta = 75.5^\circ$ is the theoretical maximum angle at which the printhead can be rotated to print the filaments side by side with $p_{\text{theo}} = 0 \mu\text{m}$. Table 1 presents a comparison between p_{theo} and experimentally measured \bar{p} from Figure 6b. For each angle, p_{theo} is calculated using Equation (9) by assuming $s = 1000 \mu\text{m}$ and $d = 250 \mu\text{m}$ (the swelling of the material exiting the nozzle is neglected here, *i.e.*, $d = D = 250 \mu\text{m}$). The experimental values \bar{p} represent an average of several pore measurements for each angle on three prints. The value $\bar{p} = 736 \mu\text{m}$ is taken directly from Case study #1 and validated with Case study #2 for $\theta = 0^\circ$ (not shown on Figure 6b). For each angle, the MAE and MRE are reported. All values of \bar{p} are smaller than p_{theo} , which could be explained by the small swelling of filaments at nozzle exit (\bar{d} increases by $\sim 4\%$ of the nozzle diameter D). The errors are relatively small ($\leq 7\%$), which is satisfactory for the variable pore size demonstration.

θ ($^\circ$)	p_{theo} (μm)	\bar{p} (μm)	$\sigma_{\bar{p}}$ (μm)	$ \bar{p} - p_{\text{theo}} $ (μm)	$ \bar{p} - p_{\text{theo}} /p_{\text{theo}}$ (%)
0	750	736	21	14	2
30	616	606	9	10	2
45	457	436	10	21	5
60	250	233	10	17	7
75.5	0	0	-	-	-

Table 1. Comparison between theoretical and experimentally measured pore size for $\theta = 0^\circ$, 30° , 45° , 60° and 75.5° .

The average printed filaments diameter \bar{d} is 250 μm (with $\sigma = 1.2 \mu\text{m}$) at $\theta = 75.5^\circ$ and was obtained by measuring the total printing width of several filaments and by dividing with the total number of measured filaments. Comparison with other measured \bar{d} (for $\theta = 30^\circ, 45^\circ$ and 60°) confirms that the printed filaments are well deposited side by side and not on top of each other. Therefore, $\bar{p} \sim 0 \mu\text{m}$ at $\theta = 75.5^\circ$. The results from Case study #2 demonstrate the multinozzle AM of microsc scaffold networks with variable pore size, which has potential for large-scale microsc scaffold requiring porosity gradients.

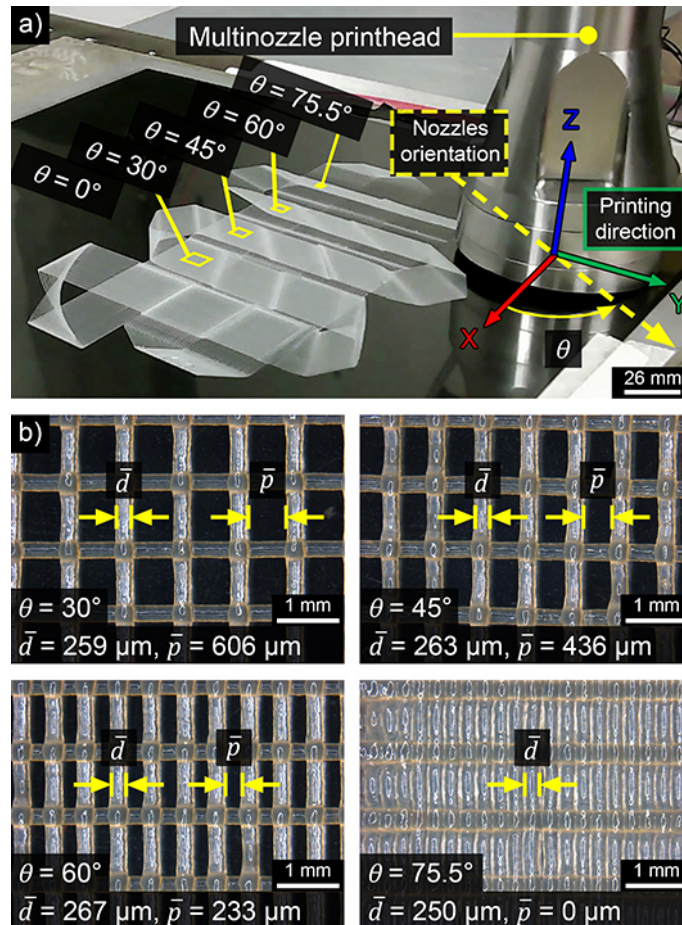


Figure 6. 2-layer microsc scaffold network (3×5 configuration) printed at 50 mm/s (~ 30 s) with variable pore size on the second layer. a) General view of the entire print. The nozzles orientation θ is given with respect to the X axis, which is perpendicular to the printing direction (Y axis). The first layer is printed at $\theta = 0^\circ$. The multinozzle is then rotated around its Z axis to increase θ (from 0° to $30^\circ, 45^\circ, 60^\circ$ and 75.5°) for each column on the second layer. b) $\times 25$ magnification images of the microsc scaffold filament stacking at $\theta = 30^\circ$ ($\bar{d} = 259 \mu\text{m}$, $\bar{p} = 606 \mu\text{m}$), $\theta = 45^\circ$ ($\bar{d} = 263 \mu\text{m}$, $\bar{p} = 436 \mu\text{m}$), $\theta = 60^\circ$ ($\bar{d} = 267 \mu\text{m}$, $\bar{p} = 233 \mu\text{m}$) and $\theta = 75.5^\circ$ ($\bar{d} = 250 \mu\text{m}$, $\bar{p} = 0 \mu\text{m}$).

4.3.3. Case study #3: Large-scale partitioned microsccaffold network

Figure 7 shows a 5-layer partitioned microsccaffold network (9×15 configuration) made of the organic ink. The target printing speed is set to $v = 50$ mm/s ($Q_{\text{tot}} \sim 63.2$ mm³/s, $\Delta P = 2.40$ MPa) in order to reduce the deceleration required for slowing down at sharp turns. Figure 7a shows the entire printed partitioned microsccaffold network. The result is a 233 mm \times 389 mm \times 1 mm network composed of 234×390 filaments wide and 135 separated microsccaffold partitions, that weighs ~ 30 g in total, and requires approximately 8 minutes 45 seconds to manufacture. Figure 7b shows the close-up top view of one of the partitioned microsccaffolds of the network. Each microsccaffold is a square of 26 mm wide surrounded by walls generated by a programmed toolpath offset. Instead of executing a sharp 90° turn to follow the programmed toolpath offset, the robot slows down, slightly round the corners of the toolpath at the wall coordinates, and travels along a diagonal path while over-extruding at the same time. Partition walls are shared among the neighboring microsccaffolds.

Figure 7c shows a $\times 25$ magnification image of the top partition wall. Filaments composing the wall have an average width $\bar{w} = 847$ μm . Over-extrusion leads to a filament with a non-circular cross-section and can be explained by a desynchronization between the robot motion speed and the printing speed. Over-extrusion of all 26 filaments results in an overall partition wall that is almost as wide as $s \sim 1$ mm. Case study #3 demonstrates the AM of a large interconnected partitioned microsccaffold network (233 mm \times 389 mm $\approx 9 \times 10^4$ mm²) in just a few minutes. The addition of partition walls shows that over-extrusion could be exploited to modify the printed filaments diameter, which could be useful for various features of large multi-functional partitioned microsccaffold applications.

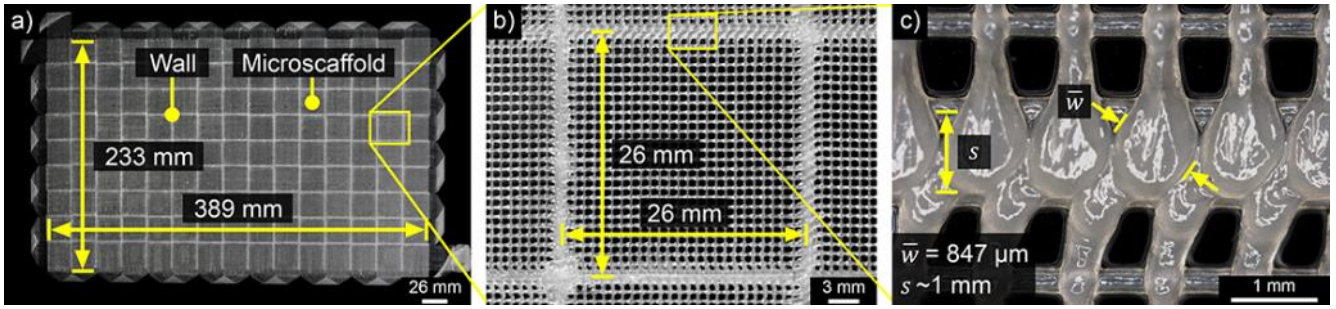


Figure 7. 5-layer partitioned microsccaffold network (9×15 configuration) printed at 50 mm/s (~ 8 min 45 s) for a total of 234×390 filaments wide and 135 microsccaffold partitions. a) Top view of the entire print. b) Close-up top view of a partitioned microsccaffold. Each microsccaffold is a square of 26 mm wide surrounded by walls, made by the offset toolpath. c) $\times 25$ magnification image of a wall. The toolpath offset leads to the robot slowing down, thus leading to over-extrusion and the printing of larger filaments ($\bar{w} = 847 \mu\text{m}$).

4.3.4. Case study #4: Thick partitioned microsccaffold network

Figure 8 shows a 50-layer partitioned microsccaffold network (3×3 configuration) made of the organic ink printed at $v = 50$ mm/s ($Q_{\text{tot}} \sim 63.2$ mm³/s, $\Delta P = 2.40$ MPa). Figure 8a shows a general view of the entire printed partitioned microsccaffold network. The print is a 77 mm \times 77 mm \times ~ 10 mm network composed of 78×78 filaments wide, that weighs ~ 30 g in total, and requires approximately 8 minutes 45 seconds to manufacture. A total of 50 layers can be achieved with the current material reservoir capacity for this 3×3 configuration. Microsccaffold cross-sections A-A, B-B and C-C were observed by micro computer tomography to assess the filament stacking quality in the various layers.

Figure 8b shows the scanned cross-section A-A. Cross-section A-A consists of the center slice of a microsccaffold with partition walls on both sides. Layers of the walls appear to be well stacked on top of each other. All 50 layers of the microsccaffold seem well connected to each other via the stacking of perpendicular filaments. Filaments located near walls appear to bend downward, which can be explained by the desynchronization between the robot motion speed and the printing speed, causing over-extrusion.

Figure 8c presents cross-sections B-B and C-C, which exhibit the filaments position across layers for a width of 7 filaments wide. Cross-section B-B shows that filaments are well aligned near the center of the microsccaffold, with an average horizontal center-to-center filament spacing $\bar{s} = 1006 \mu\text{m}$ (with $\sigma =$

57 μm). The microsccaffold also appears to slightly collapse on its own weight, as it may be observed by comparing the vertical center-to-center filament spacing z_1 (294 μm) and z_2 (422 μm). Viscoelastic properties of the ink and the large thickness of the microsccaffold can explain this behavior, as mentioned in [11]. Cross-section C-C shows that over-extruded filaments near walls are not as well aligned as in the center (B-B). The minimum measured horizontal spacing between filaments is $s_1 = 614 \mu\text{m}$ and the maximum is $s_2 = 1449 \mu\text{m}$. Despite the misalignment, the average center-to-center filament spacing $\bar{s} = 1008 \mu\text{m}$ (with $\sigma = 150 \mu\text{m}$), which is still in line with the expected geometry. Those printing defects could be minimized by reducing the programmed printing speed, thus reducing the speed difference between the microsccaffold center and the wall. It is therefore inevitable that a compromise must be achieved between the AM speed of the network and its quality. Results shown in Case study #4 exhibit the multinozzle AM of a thick periodic partitioned microsccaffold network that could prove to be useful for the rapid large-scale manufacturing of any kind of functional structures that requires a high thickness, such as the infill of a 3D-printed part.

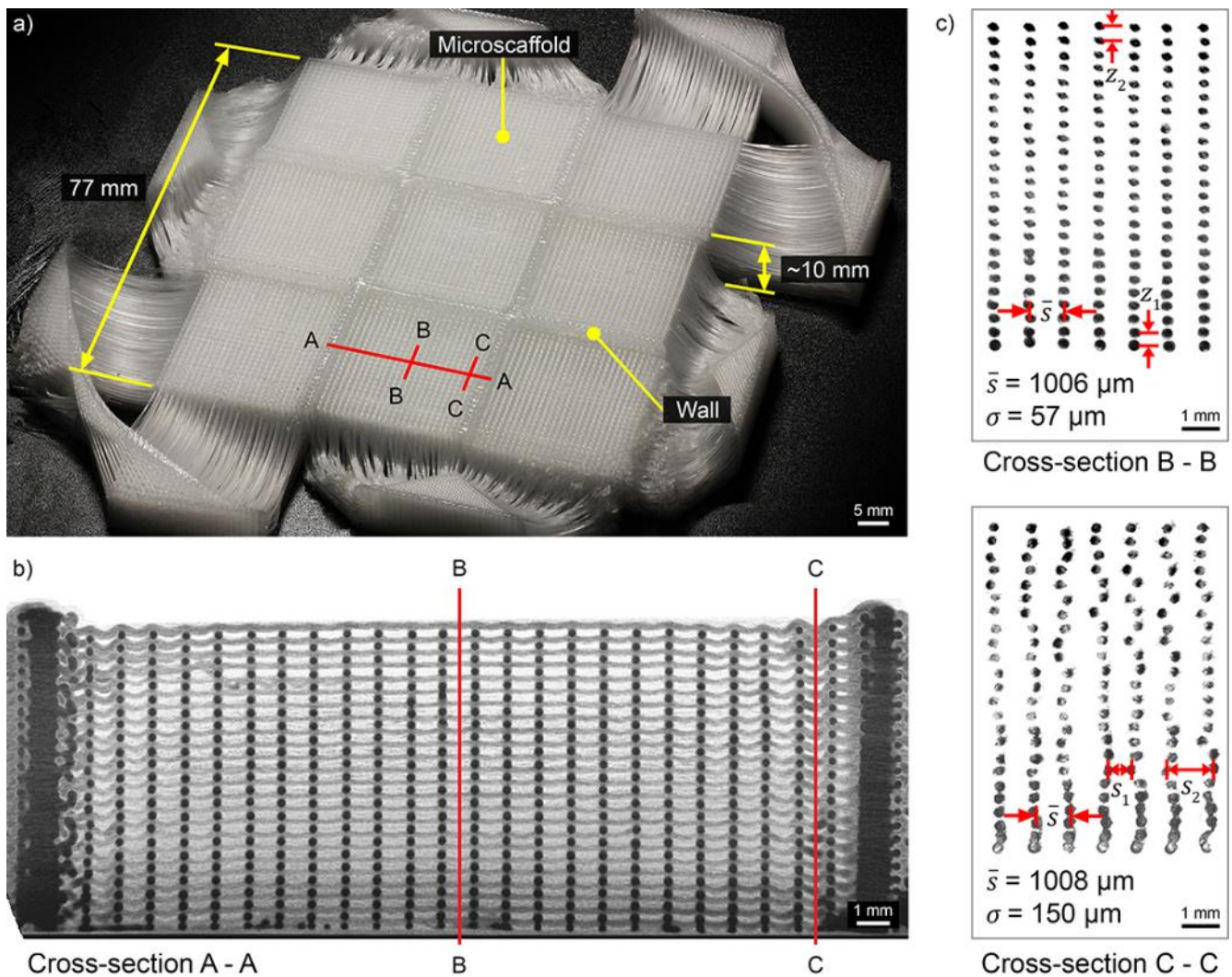


Figure 8. 50-layer partitioned microsccaffold network (3×3 configuration) printed at 50 mm/s (~ 8 min 45s) for a total of 78×78 filaments wide and 9 microscaffolds. a) General view of the entire print. Sections A-A, B-B and C-C were observed using an X-ray micro computer tomography scanner. b) Cross-sectional image of the network showing a printed microsccaffold between two partition walls (A-A). c) Cross-sectional images of filaments position across layers for a width of 7 in-plane filaments near the microsccaffold center (B-B) where $\bar{s} = 1006 \mu\text{m}$ (with $\sigma = 57 \mu\text{m}$), and near one of the wall (C-C) where $\bar{s} = 1008 \mu\text{m}$ (with $\sigma = 150 \mu\text{m}$). $s_1 = 614 \mu\text{m}$ is the minimum horizontal spacing between filaments and $s_2 = 1449 \mu\text{m}$ is the maximum. Vertical spacing $z_1 = 294 \mu\text{m} < z_2 = 422 \mu\text{m}$ shows the slight collapsing of the microsccaffold. Images c) and d) were digitally post-processed to hide the background and improve clarity of the desired features.

5. Conclusion

The development of a 6-DOF robotic AM infrastructure equipped with a custom-made multinozzle printhead combined to a high pressure system allowed the high-speed multinozzle AM of relatively large microsccaffold networks made of an organic paste-like ink. The multinozzle extrusion process is modeled by developing a Multinozzle Extrusion Prediction Model (MEPM) based on capillary rheometry.

Extrusion pressure gradient and volumetric flow rate predictions were made for printing speeds of 50, 100, 150, 200 and 250 mm/s. The MEPM is also used to explore various design configurations of multinozzle printhead. The extrusion ΔP increases as nozzles diameter D decreases or when the number of nozzles α is reduced for a given total volumetric flow rate Q_{tot} , both of which also increase the maximum reachable printing speed v . A configuration of $\alpha = 26$ nozzles, $D = 250 \mu\text{m}$ and $L = 6.5 \text{ mm}$ was selected to reach a maximum $Q_{\text{tot}} \sim 319.4 \text{ mm}^3/\text{s}$ at $v_{\text{max}} = 250 \text{ mm/s}$. To better control the extrusion process, a prediction of the material's viscosity evolution over time should also be included in the MEPM to monitor the change in pressure required for long duration extrusion, *e.g.*, time dependent curing material systems, such as epoxies.

Four case studies demonstrate the advantages of the high-speed multinozzle AM for large-scale microsc scaffold networks. Case study #1 showcased the high-speed AM of a large microsc scaffold network at a printing speed of 250 mm/s, which results in a printing time of $\sim 1 \text{ min } 36 \text{ s}$ (vs. ~ 41 minutes for a single nozzle). Case study #2 showed a microsc scaffold network with variable pore size, which could be beneficial for applications requiring a porosity gradient, *e.g.*, broadband sound absorption [32]. Case study #3 presented a large partitioned microsc scaffold network. A toolpath offset is sufficient to rapidly produce partition walls that separate all zones within the microsc scaffold network. These findings could be helpful to quickly print the infill pattern of a hollow 3D-printed part using a functional resin (*e.g.*, epoxy-based polymer) in just a few minutes. Case study #4 displayed a thick 50-layer partitioned microsc scaffold network, which demonstrated the high quality of the filament stacking. An average center-to-center spacing of $\bar{s} = 1006 \mu\text{m}$ ($\sigma = 57 \mu\text{m}$) at the microsc scaffold center and $\bar{s} = 1008 \mu\text{m}$ ($\sigma = 150 \mu\text{m}$) near walls indicate an excellent filament alignment through the layers. Yet, some extrusion control would be required to limit over-extrusion as much as possible in the transition between the printing of microsc scaffolds and surrounding walls. The impacts of the current article could also benefit other fields, such as the large-scale multinozzle AM of microvascular networks [33,34], the high-speed infill of

hollow 3D printed parts combined with the Fused Filament Fabrication technique [35] or even the large-scale AM of piezoelectric actuator meshes, similar to microscaffolds networks, for smart materials and structures [36,37]. The previously mentioned fields could all benefit from the proposed MEPM and multinozzle additive manufacturing workflow by reducing the production time of their additively manufactured parts, potentially allowing cost reduction at the same time. Future work will focus on the non-planar AM of thermosetting-based polymer with the objective of reducing the sound produced by aircraft components [38].

Acknowledgements

The authors acknowledge the collaboration of the company Mëkanic for manufacturing the multinozzle printhead and integration of the robotic cell, the technical assistance of Mr. Benedict Besner for programming the robotic cell data acquisition, of Mr. Benoit Bazin (Safran Composites) for his advice on the industrial robot and Ms. Marie-Hélène Bernier for the X-ray micro computer tomography scans. We also acknowledge the financial support from the FACMO Chair supported by the Natural Sciences and Engineering Research Council of Canada (NSERC, CRDPJ 514761-1), and Safran S.A.

References

- [1] ISO/ASTM 52900 Additive Manufacturing - General Principles - Terminology.pdf, ISO/ASTE International, Switzerland, 2015.
- [2] T. Wohlers, T. Gornet, History of additive manufacturing, (2016) 38.
- [3] R.D. Farahani, D. Therriault, M. Dubé, S. Bodkhe, M. Mahdavi, 6.13 Additive Manufacturing of Multifunctional Nanocomposites and Composites, in: *Compr. Compos. Mater. II*, Elsevier, 2018: pp. 380–407. <https://doi.org/10.1016/B978-0-12-803581-8.10019-0>.
- [4] R.L. Truby, J.A. Lewis, Printing soft matter in three dimensions, *Nature*. 540 (2016) 371–378. <https://doi.org/10.1038/nature21003>.
- [5] K.K.B. Hon, L. Li, I.M. Hutchings, Direct writing technology—Advances and developments, *CIRP Ann.* 57 (2008) 601–620. <https://doi.org/10.1016/j.cirp.2008.09.006>.
- [6] L. Li, Q. Lin, M. Tang, A.J.E. Duncan, C. Ke, Advanced Polymer Designs for Direct-Ink-Write 3D Printing, *Chem. – Eur. J.* 25 (2019) 10768–10781. <https://doi.org/10.1002/chem.201900975>.
- [7] R.D. Farahani, L.L. Lebel, D. Therriault, Processing parameters investigation for the fabrication of self-supported and freeform polymeric microstructures using ultraviolet-assisted three-dimensional printing, *J. Micromechanics Microengineering*. 24 (2014) 055020. <https://doi.org/10.1088/0960-1317/24/5/055020>.

- [8] C. Xu, B. Quinn, L.L. Lebel, D. Therriault, G. L'Espérance, Multi-Material Direct Ink Writing (DIW) for Complex 3D Metallic Structures with Removable Supports, *ACS Appl. Mater. Interfaces*. 11 (2019) 8499–8506. <https://doi.org/10.1021/acsami.8b19986>.
- [9] E. Ghafar-Zadeh, M. Sawan, D. Therriault, A Microfluidic Packaging Technique for Lab-on-Chip Applications, *IEEE Trans. Adv. Packag.* 32 (2009) 410–416. <https://doi.org/10.1109/TADVP.2008.920655>.
- [10] R. Bey-Oueslati, S.J. Palm, D. Therriault, S. Martel, HIGH SPEED DIRECT-WRITE FOR RAPID FABRICATION OF THREE-DIMENSIONAL MICROFLUIDIC DEVICES, (2006) 8.
- [11] D. Therriault, R.F. Shepherd, S.R. White, J.A. Lewis, Fugitive Inks for Direct-Write Assembly of Three-Dimensional Microvascular Networks, *Adv. Mater.* 17 (2005) 395–399. <https://doi.org/10.1002/adma.200400481>.
- [12] B. Li, P.A. Clark, K.H. Church, Robust Direct-Write Dispensing Tool and Solutions for Micro/Meso-Scale Manufacturing and Packaging, (2007) 7.
- [13] A. Dubourg-Cassagne, Intégration de structures absorbantes acoustique innovantes au sein d'une turbosoufflante, Polytechnique Montréal, 2015.
- [14] C.J. Hansen, R. Saksena, D.B. Kolesky, J.J. Vericella, S.J. Kranz, G.P. Muldowney, K.T. Christensen, J.A. Lewis, High-throughput printing via microvascular multinozzle arrays, *Adv. Mater. Deerfield Beach Fla.* 25 (2013) 96–102. <https://doi.org/10.1002/adma.201203321>.
- [15] M.A. Skylar-Scott, J. Mueller, C.W. Visser, J.A. Lewis, Voxelated soft matter via multimaterial multinozzle 3D printing, *Nature*. 575 (2019) 330–335. <https://doi.org/10.1038/s41586-019-1736-8>.
- [16] Y.J. Yoon, M. Yon, S.E. Jung, S.K. Gupta, Development of Three-Nozzle Extrusion System for Conformal Multi-Resolution 3D Printing with a Robotic Manipulator, in: Vol. 1 39th Comput. Inf. Eng. Conf., American Society of Mechanical Engineers, Anaheim, California, USA, 2019: p. V001T02A024. <https://doi.org/10.1115/DETC2019-98069>.
- [17] S.J. Kranz, Multinozzle Printheads for 3D Printing of Viscoelastic Inks, University of Illinois at Urbana-Champaign, 2013. <http://stevecrayons.com/>.
- [18] C. Gosselin, R. Duballet, Ph. Roux, N. Gaudillière, J. Dirrenberger, Ph. Morel, Large-scale 3D printing of ultra-high performance concrete – a new processing route for architects and builders, *Mater. Des.* 100 (2016) 102–109. <https://doi.org/10.1016/j.matdes.2016.03.097>.
- [19] R.A. Buswell, W.R. Leal de Silva, S.Z. Jones, J. Dirrenberger, 3D printing using concrete extrusion: A roadmap for research, *Cem. Concr. Res.* 112 (2018) 37–49. <https://doi.org/10.1016/j.cemconres.2018.05.006>.
- [20] L. Griffiths, Certified 3D printed WAAMPeller signals future for marine parts on demand, *TCT Mag.* (2017). <https://www.tctmagazine.com/api/content/f9d8bb4a-d69e-11e7-8990-121bebc5777e/> (accessed March 18, 2020).
- [21] L. Yuan, Z. Pan, D. Ding, Z. Yu, S. van Duin, H. Li, W. Li, J. Norrish, Fabrication of metallic parts with overhanging structures using the robotic wire arc additive manufacturing, *J. Manuf. Process.* (2020). <https://doi.org/10.1016/j.jmapro.2020.03.018>.
- [22] Y. Li, X. Qin, Q. Wu, Z. Hu, T. Shao, Fabrication of curved overhanging thin-walled structure with robotic wire and arc additive manufacturing (RWAAM), *Ind. Robot Int. J. Robot. Res. Appl.* 47 (2019) 102–110. <https://doi.org/10.1108/IR-05-2019-0112>.
- [23] P.M. Bhatt, A.M. Kabir, R.K. Malhan, B. Shah, A.V. Shembekar, Y.J. Yoon, S.K. Gupta, A Robotic Cell for Multi-Resolution Additive Manufacturing, in: 2019 Int. Conf. Robot. Autom. ICRA, 2019: pp. 2800–2807. <https://doi.org/10.1109/ICRA.2019.8793730>.
- [24] D. Kraljić, M. Štefanič, R. Kamnik, 3D Printing with 6D of Freedom: Controlling Material Extrusion Speed, in: K. Berns, D. Görges (Eds.), *Adv. Serv. Ind. Robot.*, Springer International Publishing, Cham, 2020: pp. 170–178. https://doi.org/10.1007/978-3-030-19648-6_20.

- [25] N.R. Fry, R.C. Richardson, J.H. Boyle, Robotic additive manufacturing system for dynamic build orientations, *Rapid Prototyp. J.* ahead-of-print (2020). <https://doi.org/10.1108/RPJ-09-2019-0243>.
- [26] D. Therriault, Directed Assembly of Three-Dimensional Microvascular Networks, University of Illinois at Urbana-Champaign, 2003.
- [27] Handling tool setup and operation manual, FANUC America Corporation, Rochester Hills, Michigan, 2018.
- [28] J. Bruneaux, D. Therriault, M.-C. Heuzey, Micro-extrusion of organic inks for direct-write assembly, *J. Micromechanics Microengineering.* 18 (2008) 115020. <https://doi.org/10.1088/0960-1317/18/11/115020>.
- [29] F.A. Morrison, Understanding rheology, Oxford University Press, New York, 2001.
- [30] S.-Z. Guo, M.-C. Heuzey, D. Therriault, Properties of Polylactide Inks for Solvent-Cast Printing of Three-Dimensional Freeform Microstructures, *Langmuir.* 30 (2014) 1142–1150. <https://doi.org/10.1021/la4036425>.
- [31] V. Tlach, Z. Ságová, I. Kuric, Circular and quasi-circular paths for the industrial robots measuring with the Renishaw Ballbar QC20-W, *MATEC Web Conf.* 254 (2019) 05007. <https://doi.org/10.1051/mateconf/201925405007>.
- [32] J. Boulvert, T. Cavalieri, J. Costa-Baptista, L. Schwan, V. Romero-García, G. Gabard, E.R. Fotsing, A. Ross, J. Mardjono, J.-P. Groby, Optimally graded porous material for broadband perfect absorption of sound, *J. Appl. Phys.* 126 (2019) 175101. <https://doi.org/10.1063/1.5119715>.
- [33] C.J. Hansen, W. Wu, K.S. Toohey, N.R. Sottos, S.R. White, J.A. Lewis, Self-Healing Materials with Interpenetrating Microvascular Networks, *Adv. Mater.* 21 (2009) 4143–4147. <https://doi.org/10.1002/adma.200900588>.
- [34] G. Postiglione, M. Alberini, S. Leigh, M. Levi, S. Turri, Effect of 3D-Printed Microvascular Network Design on the Self-Healing Behavior of Cross-Linked Polymers, *ACS Appl. Mater. Interfaces.* 9 (2017) 14371–14378. <https://doi.org/10.1021/acsami.7b01830>.
- [35] A. Papacharalampopoulos, H. Bikas, P. Stavropoulos, Path planning for the infill of 3D printed parts utilizing Hilbert curves, *Procedia Manuf.* 21 (2018) 757–764. <https://doi.org/10.1016/j.promfg.2018.02.181>.
- [36] S. Bodkhe, G. Turcot, F.P. Gosselin, D. Therriault, One-Step Solvent Evaporation-Assisted 3D Printing of Piezoelectric PVDF Nanocomposite Structures, *ACS Appl. Mater. Interfaces.* 9 (2017) 20833–20842. <https://doi.org/10.1021/acsami.7b04095>.
- [37] T. Yamashita, T. Kobayashi, Smart Table Tennis Racket Using a Rubber Mounted Ultrathin Piezoelectric Sensor Array, *Sens. Mater.* 33 (2021) 1081. <https://doi.org/10.18494/SAM.2021.2954>.
- [38] D. Brzeski, I.L. Hia, J.-F. Chauvette, R.D. Farahani, N. Piccirelli, A. Ross, D. Therriault, Design of thermoset composites for high-speed additive manufacturing of lightweight sound absorbing micro-scaffolds, *Addit. Manuf.* 47 (2021) 102245. <https://doi.org/10.1016/j.addma.2021.102245>.